Thesis for the Degree of Master of Science

Magnetic Field Structure in the Star Forming Cloud L1641

Jungmi Kwon

Department of Astronomy and Space Science

Graduate School

Kyung Hee University

Seoul, Korea

February, 2009

Magnetic Field Structure in the Star Forming Cloud L1641

Jungmi Kwon

Department of Astronomy and Space Science

Graduate School

Kyung Hee University

Seoul, Korea

February, 2009

Magnetic Field Structure in the Star Forming Cloud L1641

by

Jungmi Kwon

advided by

Dr. Soojong Pak

and

Dr. Minho Choi

Submitted to the Department of Astronomy and Space Science
and the Faculty of the Graduate School of Kyung Hee University
in partial fulfillment of the requirement for degree of
Master of Science

Dissertation Committee

....
Dr. Soojong Pak

....
Dr. Sang Joon Kim

....
Dr. Minho Choi

Magnetic Field Structure in the Star Forming Cloud L1641

ABSTRACT

We present deep and wide-field near-IR imaging polarimetry toward the HH 1-2 region in the L1641 molecular cloud. We obtained data using the JHK_s-simultaneous imaging polarimeter SIRPOL on the Infrared Survey Facility 1.4 m telescope at the South African Astronomical Observatory. We performed aperture polarimetry for the point-like sources in order to measure their integrated polarization. We detected 79 point-like sources in the J, H, and K_s bands. We found that most of the near-IR polarizations seems dichroic origin, indicating that they trace the direction of projected magnetic fields in this region. The average position angle of the projected magnetic fields is found to be about 110° in all three bands. We also suggest that the magnetic field strength in L1641 is about 100 μG, based on the modified Chandrasekhar-Fermi formula.

Contents

1. INTRODUCTION

Magnetic fields play a crucial role in various astrophysical processes, including star formation, accretion of matter, transport processes, and cosmic rays (Lazarian 2007). Magnetic fields are also thought to play a significant role in the evolution of interstellar molecular clouds (Lai et al. 2008; Mouschovias & Ciolek 1999; Shu et al. 1999). One of the problems related to star formation concerns the competition between magnetic and turbulent pressures (Alves et al. 2008). The magnetic field direction can be measured by observing the dichroic polarization of background stars in the optical and near-IR bands and/or the linearly polarized emission from the aligned dust grains in the mid-IR and far-IR bands. Near-IR imaging polarimetry is particularly useful in tracing dichroic polarization of background or embedded stars (Kandori et al. 2007), because of its low extinction. The large-scale alignment of dust grains with the Galactic magnetic field is known to be the cause of the dichroic extinction and the interstellar polarization seen in the direction of background sources. An emissive polarized component is also present in many star-forming regions in the mid-infrared, dominating at far-infrared wavelengths (Gonatas et al. 1990; Aitken et al. 1993). Since dichroic extinction is expected to result in a different wavelength dependence compared to that arising from scattering processes, a potentially important tool for discriminating between the two mechanisms is the use of multiwavelength polarimetry (Casali 1995). The possible importance of magnetic fields for bipolar outflows is suggested by polarization measurements which indicate an ambient magnetic field aligned with bipolar axis (Strom & Strom 1986).

The L1641 cloud is situated about 3° south-east of the Orion nebula (Casali 1995), and is one of the nearest giant molecular clouds (GMCs) (Sakamoto 1997). Menten et al. (2007) have determined the distance to the Orion nebular to be 414 $\pm$ 7 pc, consistented with Hirota et al. (2007) and Sandstrom et al. (2007). The L1641 cloud has been observed in molecular lines to study its structure, kinematics, and physical conditions and their relation to the initial masses and the birthrate of stars (see, e.g., Sakamoto et al. 1997; Kutner et al. 1977; Maddalena et al. 1986; Bally et al. 1987; Castets et al. 1990; Fukui & Mizuno 1991; Heyer et al. 1992; Tatematsu et al.

1993; Sakamoto et al. 1994; Nakano et al. 1995). In addition, optical and near-IR polarizations of the background stars and embedded sources have been measured by and Vrba et al. 1986.

The Herbig-Haro objects HH 1 (Herbig 1951) and HH 2 (Haro 1952) are located in the L1641 molecular cloud. They are among the brightest HH objects in the sky and thus were the first such objects to be cataloged. These two emission nebulae are separated by $140''$ (0.3 pc) and their proper motions are oppositely directed (Herbig & Jones 1981). Previous radio molecular line observations suggest that the axis of molecular outflow is in the northwest-southeast direction (PA=149°, Cernicharo 1991; Torrelles et al. 1994; Choi & Zhou 1997a; Correia et al. 1997). There is a radio continuum source located in the region between HH 1 and HH 2 (Pravdo et al. 1985; Rodríguez et al. 1990). Magnetic field structure in the HH 1-2 field has been studied based on optical polarizations of a limited number of point sources. Polarimetric observations of two stars near HH 1-2 suggest that the local magnetic field is directed roughly along the axis of the HH 1-2 outflow (Strom et al. 1985). On the basis of optical polarization measurements toward eight stars, Warren-Smith & Scarrott (1999) suggested that the magnetic field appears to be oriented at PA=126° in the 10×10 arcminutes region, which is inclined by $\sim$23° with respect to the HH 1-2 outflow axis.

In this paper, we present a wide-field near-IR polarimetry of the star forming cloud L1641 around HH 1-2. In section 2, we describe the observations and data reduction. In section 3 and 4, we present the results of this study and detailed discussion. In section 5, we present a summary.

2. Observations and Data Reduction

2.1. Observations

The observations toward the HH 1-2 region were carried out on 2008 January 9 using the imaging polarimeter SIRPOL on the Infrared Survey Facility (IRSF) 1.4 m telescope at the South African Astronomical Observatory (SAAO[1]). SIRPOL consists of a single-beam polarimeter (achromatic half-wave plate rotator unit and a high-extinction-ratio wiregrid analyzer) and a JHK_s-simultaneous imaging camera SIRIUS that has three 1024 $\times$ 1024 HgCdTe infrared detectors (Nagayama et al. 2003). IRSF/SIRPOL enables deep and wide-field ($7.7' \times 7.7'$) imaging polarimetry at JHK_s simultaneously with a scale of $0.45''$ pixel^{-1}. See Kandori et al. (2006) for a detailed description of SIRPOL. We performed 20 s exposures at 4 wave-plate angles (in the sequence of 0°, 45°, 22.5°, and 67.5°) at 10 dithered positions for each set. The same observation sets were repeated 10 times toward the target object and the sky backgrounds for better signal-to-noise ratio. The total integration time was 2000 s per wave plate angle. The typical seeing size during the observations was $\sim 1.3''$ in the J band.

2.2. Data Reduction

We processed the observed data in the same manner as described in Kandori et al. (2006) using the IRAF[2] (dark-field subtraction, flat-field correction, median sky subtraction, and frame registration). Stokes parameters, I, Q, and U, are calculated as,

$$I = (I_0 + I_{22.5} + I_{45} + I_{67.5})/2 \tag{1}$$

$$Q = I_0 - I_{45} \tag{2}$$

$$U = I_{22.5} - I_{67.5} \tag{3}$$

[1]The South African Astronomical Observatory (SAAO) is the national centre for optical and infrared astronomy in South Africa. It is a facility of the National Research Foundation under the Department of Science and Technology.

[2]IRAF is distributed by the US National Optical Astronomy Observatories, which are operated by the Association of Universities for Research in Astronomy, Inc., under cooperative agreement with the National Science Foundation.

where I_a is the intensity with the half wave plate oriented at a°. The polarization degree, $P_\circ$, and the polarization position angle, θ, can be obtained using

$$P_\circ = \frac{\sqrt{Q^2 + U^2}}{I} \tag{4}$$

and

$$\theta = \frac{1}{2} \arctan \frac{U}{Q}. \tag{5}$$

3. RESULTS

Figures $1a$ and $1b$ show the J, H, and K_s color composite intensity (I) image and polarized intensity (PI) image, respectively of the $\sim8' \times \sim8'$ region (hereafter the HH 1-2 field). For source detection and photometry on the Stokes I images, we used the IRAF daophot package (Stetson 1987). We detected stars having a peak intensity greater than 10 σ above the local sky background. The false sources detected in the automatic detection were rejected and the sources missed were added by examining carefully with eyes. Since three stars, V380 Ori, C-S star, and star star #3 of Strom et al. (1985), are too bright and saturated, they are not included in our sample sources. The aperture radius was 3 pixels, and the sky annulus was set to 10 pixels with a 5 pixel width. Among the detected sources we compiled 79 sources whose photometric uncertainties are less than 0.1 mag in all three bands (see Table 1). The point-like sources and extended sources are labeled in Figure 2. We matched the pixel coordinates of the detected sources and the celestial coordinates of their counterparts in the Two Micron All Sky Survey (2MASS) Point Source Catalogue[3]. The IRAF imcoords package was applied to the matched list in order to obtain plate transform parameters. The uncertainty in coordinate transformation is $\sim0.1''$ (rms). The magnitude and color of the photometry were calibrated using the 2MASS All Sky Point Source Catalog transformed into the 2MASS system using:

$$\mathrm{MAG}_{\mathrm{2MASS}} = \mathrm{MAG}_{\mathrm{IRSF}} + \alpha_1 \times \mathrm{COLOR}_{\mathrm{IRSF}} + \beta_1 \tag{6}$$

$$\mathrm{COLOR}_{\mathrm{2MASS}} = \alpha_2 \times \mathrm{COLOR}_{\mathrm{IRSF}} + \beta_2, \tag{7}$$

where $\mathrm{MAG}_{\mathrm{IRSF}}$ is the instrumental magnitude from the IRSF images and $\mathrm{MAG}_{\mathrm{2MASS}}$ is the magnitude from the 2MASS All Sky Point Source Catalog. Fitting the data using a robust least absolute deviation method gives α_1 = 0.015, -0.043, and 0.006, and β_1 = -4.978, -4.726, and -5.376 for J, H, and K_s, respectively, and α_2 = 1.004 and 0.963, and β_2 = -0.253 and 0.660 for

[3]This publication makes use of data products from the Two Micron All Sky Survey (2MASS), which is a joint project of the University of Massachusetts and the Infrared Processing and Analysis Center/California Institute of Technology, funded by the National Aeronautics and Space Administration and the National Science Foundation.

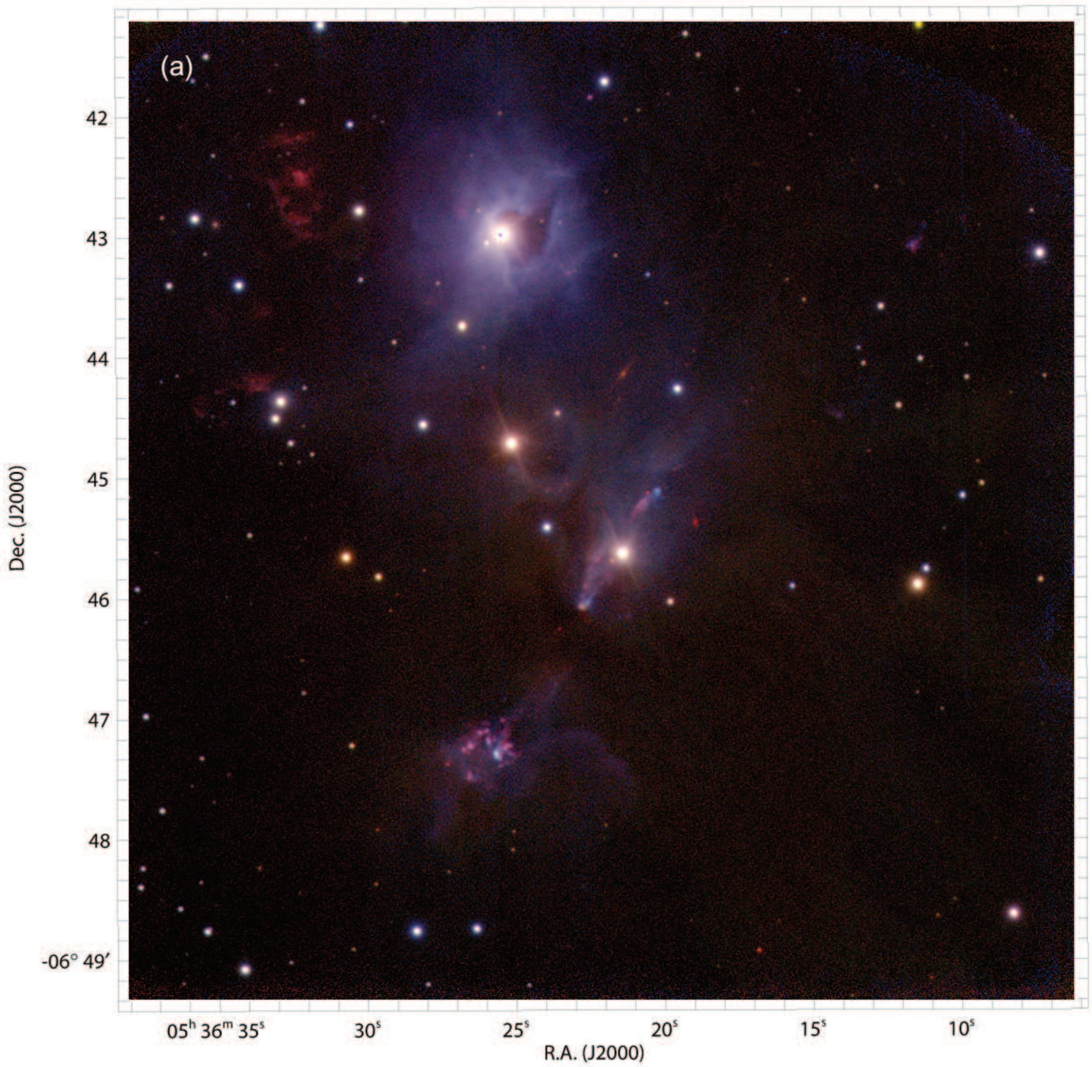

Fig. 1.— Color composite near-IR images in the J(*blue*), H(*green*), and K_s(*red*) bands. (a) Stokes I image. (b) Polarized Intensity image. The size of the field-of-view is $\sim 8' \times \sim 8'$. We note that there are bad pixel clusters on the J image around the upper-right corner and the middle of the right side.

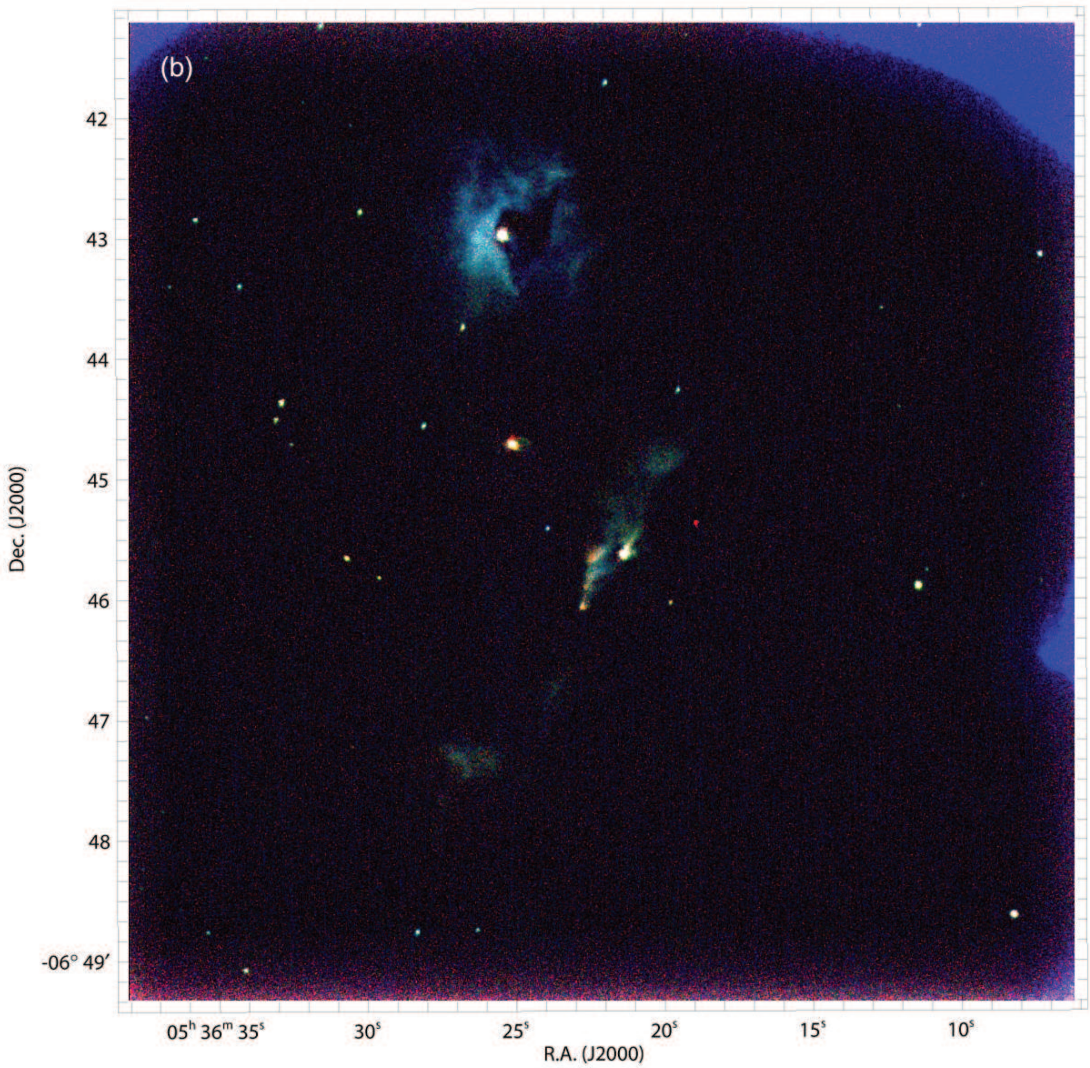

Fig. 1.— Continued

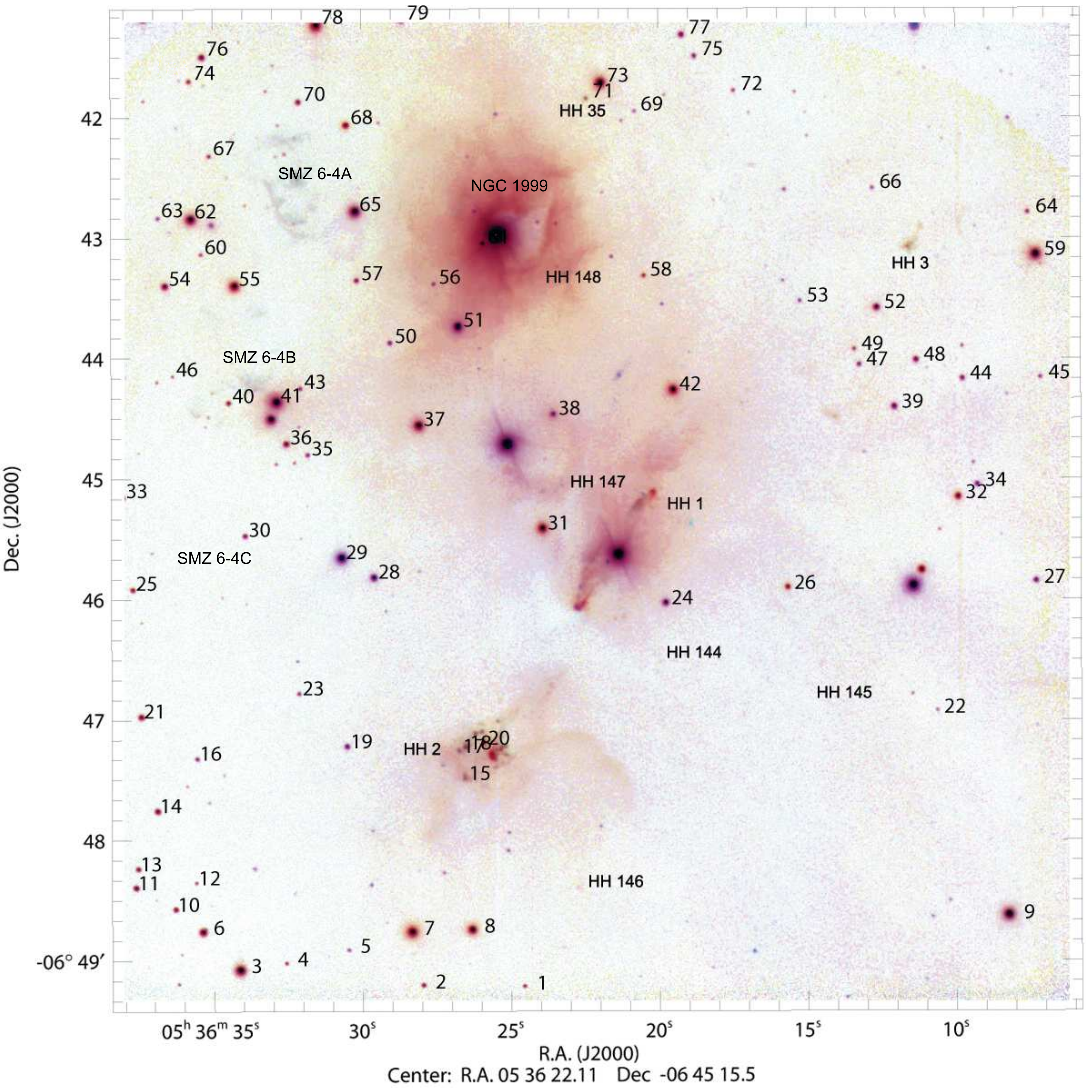

Fig. 2.— Map toward the HH 1-2 field from the IRSF 1.4 m telescope. The 79 point-like sources are numbered following Table 1. Extended sources are labeled. Herbig-Haro object numbers are from "A General Catalogue of Herbig-Haro Objects, 2nd Edition" by Reipurth. (http://casa.colorado.edu/hhcat/)

$J - H$ and $H - K_s$, respectively. Note that the coefficients β_1 and β_2 include both zero point correction and aperture correction.

We carried out aperture polarimetry of the point-like sources on the combined intensity images for each wave plate angle ($I_0 + I_{22.5} + I_{45} + I_{67.5}$). Since the center of point sources cannot be determined satisfactory on the Q and U images, we did not use the Stokes Q and U images. On the basis of aperture photometries of 79 sources on each wave plate angle image, the Stokes parameters for each source were obtained using the equations (2) and (3). The aperture and sky radius are the same as those used in the photometry of I images. Since the initial polarization degree, $P_\circ$, is a positive quantity, the derived $P_\circ$ values tend to be overestimated, especially for low signal-to-noise ratio sources. To correct for the bias, the polarization degrees were debiased (Wardle & Kronberg 1974), using the following equation:

$$P = \sqrt{P_\circ^2 - \delta P^2}, \tag{8}$$

where δP is the uncertainty in $P_\circ$. Finally, P was corrected using the polarization efficiencies of SIRPOL, i.e., 95.5%, 96.3%, and 98.5% at J, H, and K_s, respectively (Kandori et al. 2006). The polarimetry of the 79 point-like sources with JHK_s detections are shown in Table 2. For the sources with $P/\delta P \geq 4$ and $P < 9\%$ (21 sources), the correlation coefficients for (θ_H, θ_{K_s}) and (θ_H, θ_J) are 0.90 and 0.97, respectively. The linearly fitted slopes of (P_H vs. P_{K_s}) and (P_H vs. P_J) diagrams are 0.621 and 1.670, with the correlation coefficients of 0.95 and 0.97, respectively. These slopes are consistent with the empirical values of 0.61 and 1.61 from the relation $P \propto \lambda^{-\alpha}$, where α = 1.8 $\pm$ 0.2 (Whittet 1992).

Figure 3 shows a two color diagram for all of the sources detected in the J, H, and K_s bands in order to classify the sample into three groups, i.e., Dwarf+Giant stars, pre-main-sequence (PMS) stars, and Class I sources. We found 5 sources in the Class I region, 4 sources in the PMS star region , and the other 70 sources in the Dwarf+Giant star region. There is no tendency of higher polarization in earlier evolutionary stages or larger infrared excess.

Table 1. The aperture photometry of point-like sources in the HH 1-2 field

Source	Position		J (mag)	H (mag)	K_s (mag)	Classification[a]
	$\alpha_{J2000.0}$	$\delta_{J2000.0}$				
1	5 36 24.59	6 49 11.6	17.87 ± 0.04	16.650 ± 0.013	16.06 ± 0.05	Dwarf+Giant
2	5 36 27.99	6 49 11.1	17.32 ± 0.02	15.984 ± 0.007	15.34 ± 0.03	Dwarf+Giant
3	5 36 34.15	6 49 03.5	13.3732 ± 0.0006	12.2258 ± 0.0003	11.7275 ± 0.0007	Dwarf+Giant
4	5 36 32.60	6 49 00.1	18.08 ± 0.03	16.788 ± 0.009	16.28 ± 0.04	Dwarf+Giant
5	5 36 30.50	6 48 53.5	19.29 ± 0.07	17.205 ± 0.013	16.28 ± 0.03	Dwarf+Giant
6	5 36 35.41	6 48 44.6	14.7778 ± 0.0013	13.8340 ± 0.0006	13.409 ± 0.002	Dwarf+Giant
7	5 36 28.37	6 48 44.5	12.6581 ± 0.0003	12.1240 ± 0.0002	12.0333 ± 0.0006	Dwarf+Giant
8	5 36 26.35	6 48 43.4	13.5900 ± 0.0006	13.0695 ± 0.0003	12.7278 ± 0.0013	Pre-main-sequence
9	5 36 08.29	6 48 36.2	13.1827 ± 0.0004	11.9483 ± 0.0002	10.9966 ± 0.0003	Dwarf+Giant
10	5 36 36.32	6 48 33.3	16.590 ± 0.005	15.607 ± 0.002	15.171 ± 0.011	Dwarf+Giant
11	5 36 37.65	6 48 22.5	16.292 ± 0.005	14.9498 ± 0.0019	14.395 ± 0.007	Dwarf+Giant
12	5 36 35.62	6 48 20.1	18.62 ± 0.03	17.216 ± 0.011	16.46 ± 0.03	Dwarf+Giant
13	5 36 37.57	6 48 13.2	16.743 ± 0.007	15.668 ± 0.003	15.190 ± 0.014	Dwarf+Giant
14	5 36 36.92	6 47 44.4	16.257 ± 0.004	14.9504 ± 0.0017	14.410 ± 0.005	Dwarf+Giant
15	5 36 26.57	6 47 27.8	17.44 ± 0.03	16.94 ± 0.02	15.437 ± 0.019	Class I
16	5 36 35.58	6 47 18.4	18.07 ± 0.02	16.451 ± 0.006	15.674 ± 0.015	Dwarf+Giant
17	5 36 26.77	6 47 14.4	17.63 ± 0.07	17.01 ± 0.05	15.16 ± 0.03	Class I
18	5 36 26.55	6 47 12.7	16.599 ± 0.012	16.140 ± 0.011	14.65 ± 0.014	Class I
19	5 36 30.54	6 47 12.3	17.796 ± 0.016	15.409 ± 0.003	14.258 ± 0.004	Dwarf+Giant
20	5 36 25.94	6 47 10.4	16.50 ± 0.05	16.29 ± 0.05	15.24 ± 0.04	Class I
21	5 36 37.46	6 46 57.5	16.105 ± 0.004	14.7681 ± 0.0016	14.342 ± 0.006	Dwarf+Giant
22	5 36 10.68	6 46 54.3	19.44 ± 0.07	17.664 ± 0.015	16.87 ± 0.05	Dwarf+Giant
23	5 36 32.15	6 46 46.0	18.44 ± 0.03	16.723 ± 0.008	15.99 ± 0.02	Pre-main-sequence
24	5 36 19.80	6 46 00.7	16.445 ± 0.005	14.4155 ± 0.0013	13.2333 ± 0.0018	Dwarf+Giant
25	5 36 37.73	6 45 54.2	16.665 ± 0.006	15.675 ± 0.003	15.326 ± 0.018	Dwarf+Giant
26	5 36 15.70	6 45 53.1	15.793 ± 0.003	15.2623 ± 0.0018	15.035 ± 0.009	Dwarf+Giant
27	5 36 07.34	6 45 50.0	17.65 ± 0.02	15.471 ± 0.003	14.452 ± 0.006	Dwarf+Giant
28	5 36 29.62	6 45 48.2	16.511 ± 0.006	14.0196 ± 0.0007	12.8731 ± 0.0013	Dwarf+Giant
29	5 36 30.71	6 45 38.5	14.9340 ± 0.0013	12.1501 ± 0.0003	10.7675 ± 0.0003	Dwarf+Giant
30	5 36 33.95	6 45 27.5	17.461 ± 0.011	15.751 ± 0.003	15.093 ± 0.009	Dwarf+Giant
31	5 36 23.95	6 45 23.8	13.1658 ± 0.0004	12.5382 ± 0.0003	12.2845 ± 0.0008	Dwarf+Giant
32	5 36 09.96	6 45 08.1	15.1245 ± 0.0015	14.5002 ± 0.0009	14.258 ± 0.005	Dwarf+Giant
33	5 36 38.06	6 45 08.4	16.872 ± 0.009	15.694 ± 0.004	15.298 ± 0.017	Dwarf+Giant
34	5 36 09.32	6 45 02.0	17.942 ± 0.018	15.640 ± 0.003	14.607 ± 0.006	Dwarf+Giant
35	5 36 31.84	6 44 47.2	18.36 ± 0.02	16.360 ± 0.007	15.536 ± 0.015	Dwarf+Giant
36	5 36 32.56	6 44 41.7	16.288 ± 0.004	14.7617 ± 0.0018	14.083 ± 0.004	Dwarf+Giant
37	5 36 28.10	6 44 32.5	13.2042 ± 0.0004	12.2083 ± 0.0003	11.7394 ± 0.0005	Pre-main-sequence
38	5 36 23.58	6 44 27.0	17.172 ± 0.009	15.288 ± 0.003	14.027 ± 0.004	Dwarf+Giant
39	5 36 12.10	6 44 23.3	16.780 ± 0.007	14.7691 ± 0.0015	13.852 ± 0.003	Dwarf+Giant
40	5 36 34.49	6 44 21.4	17.059 ± 0.008	15.993 ± 0.003	15.523 ± 0.014	Dwarf+Giant
41	5 36 32.88	6 44 20.9	12.8645 ± 0.0006	11.3186 ± 0.0003	10.5466 ± 0.0003	Dwarf+Giant
42	5 36 19.54	6 44 14.9	13.0878 ± 0.0004	12.5083 ± 0.0003	12.2375 ± 0.0007	Dwarf+Giant
43	5 36 32.09	6 44 14.2	17.97 ± 0.03	16.449 ± 0.011	15.76 ± 0.02	Dwarf+Giant
44	5 36 09.81	6 44 09.3	17.393 ± 0.013	15.851 ± 0.004	15.141 ± 0.010	Dwarf+Giant
45	5 36 07.19	6 44 08.8	19.04 ± 0.07	16.895 ± 0.011	15.92 ± 0.02	Pre-main-sequence
46	5 36 36.38	6 44 08.1	18.99 ± 0.04	17.84 ± 0.02	16.96 ± 0.05	Dwarf+Giant
47	5 36 13.28	6 44 02.4	18.082 ± 0.019	16.140 ± 0.005	15.177 ± 0.010	Dwarf+Giant
48	5 36 11.37	6 44 00.1	16.695 ± 0.006	15.222 ± 0.002	14.545 ± 0.006	Dwarf+Giant
49	5 36 13.45	6 43 54.7	17.997 ± 0.017	16.871 ± 0.011	16.22 ± 0.03	Dwarf+Giant
50	5 36 29.06	6 43 51.5	17.838 ± 0.018	15.972 ± 0.004	15.110 ± 0.011	Dwarf+Giant
51	5 36 26.77	6 43 43.4	13.8429 ± 0.0012	11.9368 ± 0.0004	11.0684 ± 0.0003	Dwarf+Giant
52	5 36 12.69	6 43 34.0	15.818 ± 0.002	14.3380 ± 0.0009	13.636 ± 0.002	Dwarf+Giant
53	5 36 15.27	6 43 30.8	19.22 ± 0.06	17.020 ± 0.010	16.01 ± 0.02	Dwarf+Giant
54	5 36 36.63	6 43 23.2	15.718 ± 0.003	14.4132 ± 0.0011	13.877 ± 0.003	Dwarf+Giant
55	5 36 34.28	6 43 23.2	13.1717 ± 0.0004	12.4930 ± 0.0003	12.3299 ± 0.0008	Dwarf+Giant
56	5 36 27.59	6 43 22.2	18.58 ± 0.08	16.682 ± 0.014	15.93 ± 0.03	Dwarf+Giant
57	5 36 30.18	6 43 20.4	17.191 ± 0.010	15.763 ± 0.004	15.139 ± 0.009	Dwarf+Giant
58	5 36 20.52	6 43 18.1	16.913 ± 0.009	16.370 ± 0.005	16.10 ± 0.02	Dwarf+Giant
59	5 36 07.34	6 43 07.6	12.8909 ± 0.0004	11.8620 ± 0.0003	11.4164 ± 0.0005	Dwarf+Giant
60	5 36 35.42	6 43 07.5	18.70 ± 0.04	17.147 ± 0.010	16.51 ± 0.04	Dwarf+Giant
61	5 36 25.94	6 43 02.2	13.850 ± 0.016	12.998 ± 0.012	12.551 ± 0.011	Dwarf+Giant
62	5 36 35.76	6 42 49.9	13.4875 ± 0.0005	12.3635 ± 0.0003	11.9266 ± 0.0006	Dwarf+Giant
63	5 36 36.87	6 42 49.4	19.11 ± 0.05	17.016 ± 0.010	16.07 ± 0.02	Dwarf+Giant
64	5 36 07.61	6 42 46.6	18.13 ± 0.03	16.476 ± 0.006	15.733 ± 0.018	Dwarf+Giant
65	5 36 30.23	6 42 46.1	13.3086 ± 0.0005	11.8051 ± 0.0002	11.0855 ± 0.0003	Dwarf+Giant

Table 1—Continued

Source	Position		J (mag)	H (mag)	K_s (mag)	Classification[a]
	$\alpha_{J2000.0}$	$\delta_{J2000.0}$				
66	5 36 12.83	6 42 34.6	19.07 ± 0.05	17.255 ± 0.011	16.31 ± 0.03	Dwarf+Giant
67	5 36 35.14	6 42 18.6	18.25 ± 0.02	16.645 ± 0.008	16.00 ± 0.02	Dwarf+Giant
68	5 36 30.53	6 42 03.1	14.9935 ± 0.0013	14.4268 ± 0.0009	14.162 ± 0.004	Dwarf+Giant
69	5 36 20.82	6 41 56.3	19.53 ± 0.09	17.530 ± 0.019	16.71 ± 0.04	Dwarf+Giant
70	5 36 32.13	6 41 51.6	16.778 ± 0.006	15.532 ± 0.003	15.026 ± 0.008	Dwarf+Giant
71	5 36 22.45	6 41 49.9	17.78 ± 0.03	17.34 ± 0.03	15.86 ± 0.02	Class I
72	5 36 17.49	6 41 46.1	18.28 ± 0.03	17.067 ± 0.011	16.42 ± 0.03	Dwarf+Giant
73	5 36 21.96	6 41 42.0	12.8163 ± 0.0004	12.2015 ± 0.0002	11.9298 ± 0.0006	Dwarf+Giant
74	5 36 35.81	6 41 41.3	16.962 ± 0.011	16.359 ± 0.007	16.04 ± 0.03	Dwarf+Giant
75	5 36 18.80	6 41 28.9	18.055 ± 0.03	16.156 ± 0.005	15.301 ± 0.013	Dwarf+Giant
76	5 36 35.37	6 41 29.2	16.087 ± 0.006	14.8272 ± 0.0015	14.328 ± 0.006	Dwarf+Giant
77	5 36 19.23	6 41 18.2	16.690 ± 0.011	15.147 ± 0.003	14.457 ± 0.008	Dwarf+Giant
78	5 36 31.52	6 41 13.6	12.7228 ± 0.0005	11.9566 ± 0.0003	11.7781 ± 0.0008	Dwarf+Giant
79	5 36 28.66	6 41 11.3	17.20 ± 0.020	15.332 ± 0.005	14.489 ± 0.010	Dwarf+Giant

Note. — Units of right ascension are hours, minutes, and seconds, and units of declination are degrees, arcminutes, and arcseconds. Positions are from the JHK_s image (Fig. 1).

[a]Classification according to the two color diagram (Fig. 3).

Table 2. Polarimetry of the point-like sources in the HH 1-2 field

Source	P_J (%)	P_H (%)	P_{K_s} (%)	θ_J (°)	θ_H (°)	θ_{K_s} (°)
1	8.3 ± 4.3	6.5 ± 2.1	6.9 ± 6.9	8.1 ± 13.2	148.2 ± 8.8	87.0 ± 81.5
2	2.8 ± 3.3	3.7 ± 1.1	8.4 ± 3.3	161.6 ± 21.7	113.2 ± 7.9	103.3 ± 10.5
3	2.73 ± 0.08	2.27 ± 0.04	1.55 ± 0.09	97.8 ± 0.8	95.8 ± 0.5	83.5 ± 1.6
4	5.9 ± 3.1	1.1 ± 1.5	13.0 ± 4.9	99.3 ± 13.4	21.8 ± 22.8	22.5 ± 10.1
5	30.9 ± 10.3	5.4 ± 1.8	6.5 ± 4.2	51.2 ± 9.1	112.0 ± 9.0	177.9 ± 15.6
6	2.83 ± 0.17	2.20 ± 0.09	1.1 ± 0.3	121.7 ± 1.7	121.6 ± 1.2	111.6 ± 6.9
7	0.31 ± 0.04	0.44 ± 0.03	0.41 ± 0.08	107.6 ± 3.7	121.4 ± 2.0	94.6 ± 5.6
8	0.35 ± 0.07	0.69 ± 0.05	0.41 ± 0.16	116.4 ± 5.9	109.8 ± 2.1	124.7 ± 10.4
9	10.96 ± 0.06	9.41 ± 0.03	7.31 ± 0.04	148.55 ± 0.15	147.66 ± 0.08	147.89 ± 0.15
10	4.4 ± 0.7	3.4 ± 0.3	2.8 ± 1.4	143.3 ± 4.7	128.1 ± 2.9	142.4 ± 12.9
11	2.5 ± 0.6	2.1 ± 0.3	0.9 ± 0.9	119.3 ± 6.9	115.8 ± 3.7	109.6 ± 42.7
12	10.6 ± 4.6	2.4 ± 1.7	7.2 ± 4.4	162.2 ± 11.5	127.7 ± 16.5	132.9 ± 14.9
13	6.0 ± 0.9	4.2 ± 0.5	2.5 ± 1.8	117.8 ± 4.1	117.0 ± 3.6	103.0 ± 16.4
14	1.8 ± 0.6	2.0 ± 0.2	1.2 ± 0.7	124.6 ± 8.5	125.8 ± 3.4	89.6 ± 14.4
15	3.8 ± 2.3	3.8 ± 2.2	2.5 ± 1.9	41.6 ± 14.9	49.6 ± 14.2	9.9 ± 17.1
16	7.0 ± 2.8	3.1 ± 0.8	4.6 ± 2.0	117.7 ± 10.7	124.2 ± 7.3	112.7 ± 11.3
17	5.2 ± 5.2	9.5 ± 4.3	7.2 ± 2.8	70.7 ± 59.7	136.0 ± 11.8	140.4 ± 10.4
18	3.7 ± 1.1	1.1 ± 1.1	0.9 ± 1.2	57.8 ± 8.2	139.7 ± 33.0	138.8 ± 22.3
19	7.5 ± 2.1	3.1 ± 0.3	2.9 ± 0.6	129.0 ± 7.7	132.8 ± 3.2	118.1 ± 5.5
20	5.7 ± 5.7	5.7 ± 4.8	3.1 ± 4.3	100.1 ± 116.6	136.8 ± 18.5	146.6 ± 23.2
21	4.5 ± 0.5	3.3 ± 0.2	3.2 ± 0.7	115.9 ± 3.1	118.7 ± 2.1	123.4 ± 6.3
22	10.0 ± 10.0	4.6 ± 2.3	6.2 ± 6.2	111.9 ± 20.2	82.7 ± 12.8	22.8 ± 48.3
23	3.4 ± 3.4	7.3 ± 1.2	6.5 ± 2.9	164.9 ± 32.8	132.1 ± 4.9	157.3 ± 11.7
24	7.8 ± 0.6	6.06 ± 0.16	3.9 ± 0.2	20.0 ± 2.2	20.9 ± 0.7	13.6 ± 1.7
25	1.8 ± 0.9	2.8 ± 0.5	1.9 ± 2.2	148.4 ± 13.0	118.4 ± 5.3	144.5 ± 21.4
26	0.8 ± 0.4	0.4 ± 0.3	1.8 ± 1.2	170.0 ± 13.1	104.2 ± 16.2	88.3 ± 15.6
27	4.4 ± 2.8	4.3 ± 0.4	4.7 ± 0.8	89.2 ± 15.5	84.6 ± 2.7	83.8 ± 4.8
28	7.0 ± 0.7	5.01 ± 0.10	3.21 ± 0.16	100.5 ± 2.9	106.4 ± 0.6	108.1 ± 1.4
29	5.85 ± 0.18	4.05 ± 0.03	2.59 ± 0.03	114.6 ± 0.9	113.7 ± 0.2	112.0 ± 0.3
30	7.4 ± 1.6	4.5 ± 0.5	1.6 ± 1.2	118.7 ± 5.9	126.8 ± 2.9	132.3 ± 16.9
31	0.51 ± 0.05	0.75 ± 0.04	0.49 ± 0.10	118.9 ± 3.0	113.1 ± 1.5	100.7 ± 5.5
32	0.6 ± 0.2	0.65 ± 0.16	2.5 ± 0.6	106.6 ± 9.3	123.5 ± 6.7	66.1 ± 6.5
33	5.1 ± 1.4	1.9 ± 0.7	8.3 ± 2.3	115.2 ± 7.4	130.8 ± 9.5	137.8 ± 7.7
34	13.7 ± 2.5	5.1 ± 0.4	3.5 ± 0.8	79.2 ± 5.2	82.6 ± 2.3	74.2 ± 6.1
35	6.4 ± 3.2	5.9 ± 0.9	1.9 ± 1.9	153.4 ± 12.9	114.7 ± 4.4	151.8 ± 44.0
36	6.4 ± 0.5	5.2 ± 0.2	4.0 ± 0.5	125.5 ± 2.2	115.3 ± 1.1	130.4 ± 3.4
37	0.72 ± 0.05	0.82 ± 0.03	0.64 ± 0.06	71.5 ± 2.1	70.9 ± 1.1	70.7 ± 2.8
38	1.2 ± 1.2	0.4 ± 0.3	1.7 ± 0.5	17.8 ± 31.1	132.4 ± 18.9	118.9 ± 8.3
39	2.8 ± 0.8	2.3 ± 0.2	1.9 ± 0.4	124.8 ± 8.3	111.5 ± 2.7	108.6 ± 5.8
40	3.9 ± 1.0	3.1 ± 0.5	2.9 ± 1.9	107.7 ± 6.9	113.2 ± 4.6	48.9 ± 15.7
41	1.58 ± 0.05	1.38 ± 0.03	0.95 ± 0.03	132.5 ± 1.0	128.1 ± 0.6	126.0 ± 0.9
42	0.55 ± 0.05	0.65 ± 0.04	0.48 ± 0.09	114.7 ± 2.8	115.1 ± 1.6	110.3 ± 5.4
43	1.5 ± 2.8	4.9 ± 1.2	5.0 ± 2.5	115.3 ± 25.2	112.9 ± 6.7	144.6 ± 12.8
44	2.8 ± 1.5	2.4 ± 0.5	3.3 ± 1.3	108.0 ± 13.2	108.5 ± 5.4	135.9 ± 10.6
45	17.8 ± 8.9	5.9 ± 1.7	3.2 ± 3.2	148.2 ± 12.8	125.6 ± 7.8	168.1 ± 52.7
46	1.78 ± 5.02	3.8 ± 3.3	9.3 ± 7.0	103.5 ± 27.0	27.0 ± 18.9	3.1 ± 17.3
47	11.3 ± 2.5	5.3 ± 0.7	3.6 ± 1.4	84.1 ± 6.1	107.2 ± 3.9	104.5 ± 10.3
48	3.3 ± 0.8	2.0 ± 0.3	1.6 ± 0.8	86.8 ± 6.3	113.6 ± 4.0	107.2 ± 12.3
49	17.8 ± 2.6	9.1 ± 1.3	7.9 ± 3.4	149.9 ± 4.1	135.1 ± 4.0	112.2 ± 11.3
50	2.5 ± 2.5	5.1 ± 0.6	3.2 ± 1.3	144.4 ± 34.9	104.6 ± 3.3	108.3 ± 10.5
51	1.67 ± 0.11	1.10 ± 0.04	0.58 ± 0.04	90.1 ± 1.8	91.7 ± 1.0	110.2 ± 1.9
52	4.7 ± 0.4	3.01 ± 0.14	1.6 ± 0.3	87.3 ± 2.2	95.8 ± 1.3	98.0 ± 5.5
53	2.3 ± 7.3	2.2 ± 1.4	3.0 ± 3.0	22.8 ± 27.3	109.1 ± 15.5	42.7 ± 52.8
54	3.5 ± 0.3	2.48 ± 0.16	1.7 ± 0.4	131.7 ± 2.8	122.6 ± 1.9	138.2 ± 6.7
55	0.66 ± 0.05	0.71 ± 0.04	0.6 ± 0.1	125.4 ± 2.3	120.5 ± 1.4	111.3 ± 4.6
56	15.4 ± 6.0	8.2 ± 1.4	9.0 ± 2.9	112.3 ± 10.4	105.9 ± 4.9	129.2 ± 8.6
57	2.9 ± 1.2	3.4 ± 0.5	0.7 ± 1.2	142.0 ± 11.2	111.3 ± 4.2	78.0 ± 25.3
58	1.0 ± 1.0	2.4 ± 0.8	0.3 ± 3.1	100.5 ± 42.2	102.9 ± 8.9	47.1 ± 28.5
59	4.14 ± 0.05	2.54 ± 0.03	1.40 ± 0.06	92.8 ± 0.3	95.0 ± 0.4	103.5 ± 1.2
60	4.3 ± 4.6	1.8 ± 1.7	6.6 ± 4.5	8.4 ± 20.8	162.9 ± 19.2	150.2 ± 16.2
61	1.2 ± 1.2	0.1 ± 0.9	0.4 ± 0.8	155.8 ± 31.1	151.7 ± 28.5	115.8 ± 25.9
62	2.33 ± 0.07	1.71 ± 0.04	1.08 ± 0.07	130.4 ± 0.8	125.3 ± 0.6	114.3 ± 1.9
63	5.8 ± 5.8	6.5 ± 1.5	2.8 ± 3.3	24.7 ± 74.2	139.5 ± 6.4	34.7 ± 21.9
64	8.0 ± 3.6	2.4 ± 0.9	2.2 ± 2.2	128.1 ± 11.6	64.2 ± 10.6	178.9 ± 31.8
65	1.45 ± 0.06	1.17 ± 0.03	0.81 ± 0.04	126.4 ± 1.2	128.5 ± 0.6	138.7 ± 1.3

Table 2—Continued

Source	P_J (%)	P_H (%)	P_{K_s} (%)	θ_J ($^\circ$)	θ_H ($^\circ$)	θ_{K_s} ($^\circ$)
66	16.4 ± 5.8	2.6 ± 1.6	3.8 ± 3.8	93.9 ± 9.5	14.7 ± 14.9	74.0 ± 52.9
67	14.19 ± 3.09	1.8 ± 1.3	4.2 ± 2.9	121.2 ± 6.1	138.3 ± 16.4	158.4 ± 16.3
68	0.25 ± 0.18	0.56 ± 0.15	2.1 ± 0.5	124.9 ± 16.6	98.4 ± 7.5	124.1 ± 6.9
69	19.9 ± 11.1	6.7 ± 2.5	5.4 ± 5.4	140.5 ± 14.0	43.9 ± 10.0	145.6 ± 58.4
70	7.2 ± 0.8	4.3 ± 0.4	2.2 ± 1.2	115.8 ± 3.2	117.8 ± 2.6	148.0 ± 13.1
71	5.2 ± 2.5	2.4 ± 2.9	2.5 ± 2.5	29.3 ± 12.6	53.2 ± 22.0	141.9 ± 28.9
72	9.5 ± 3.1	1.5 ± 1.5	13.4 ± 4.3	34.9 ± 8.9	75.5 ± 20.4	101.3 ± 8.8
73	0.4 ± 0.05	0.61 ± 0.03	0.44 ± 0.07	135.7 ± 3.1	134.6 ± 1.5	132.8 ± 4.7
74	0.5 ± 1.4	0.9 ± 0.9	8.9 ± 3.1	132.4 ± 27.1	104.0 ± 35.2	118.1 ± 9.3
75	3.9 ± 3.3	5.1 ± 0.8	1.7 ± 1.7	67.1 ± 18.6	101.0 ± 4.2	90.9 ± 37.5
76	2.8 ± 0.8	3.5 ± 0.2	0.7 ± 0.7	122.3 ± 7.5	120.7 ± 2.0	88.3 ± 21.1
77	8.9 ± 1.4	4.6 ± 0.4	4.7 ± 1.1	87.7 ± 4.4	101.0 ± 2.6	123.0 ± 6.3
78	0.59 ± 0.06	0.51 ± 0.03	0.24 ± 0.12	109.8 ± 2.8	105.3 ± 1.9	120.6 ± 12.3
79	9.0 ± 2.4	5.1 ± 0.7	1.4 ± 1.4	118.8 ± 7.4	122.5 ± 3.7	84.8 ± 36.3

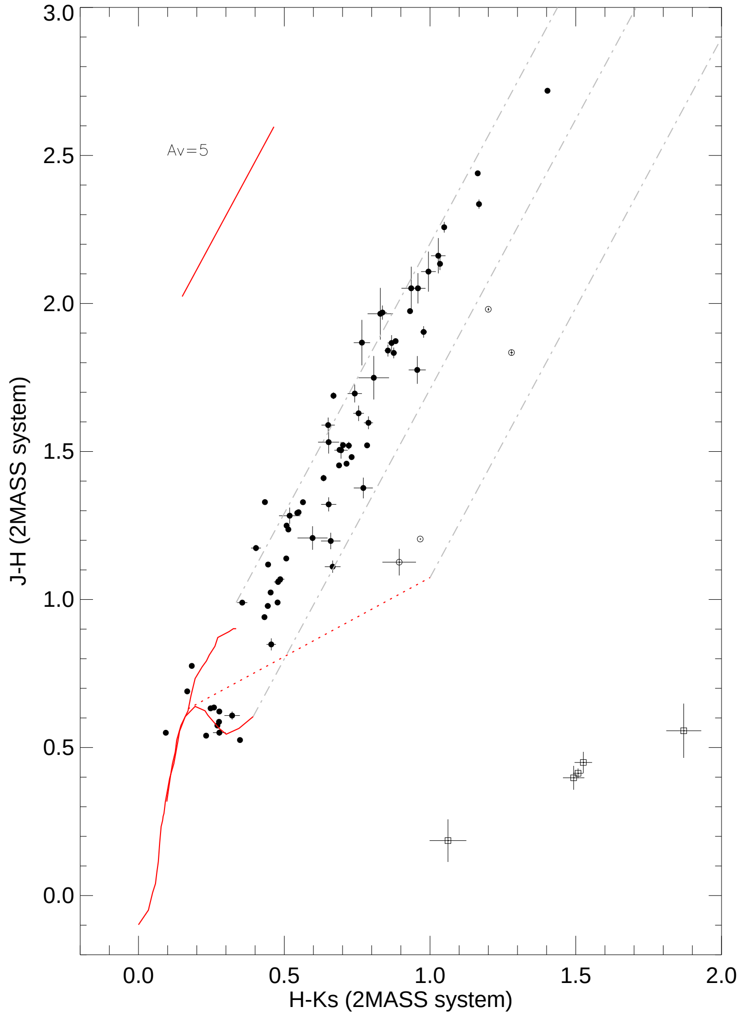

Fig. 3.— Two color diagram of the point-like sources in the HH 1-2 field. The red solid curve shows the infrared color of the main sequence and giant branch (Bessell & Brett 1988), and the red dotted line is T Tauri locus from Meyer et al. (1997). The grey dash-dotted line separates the sources with infrared excesses from the reddened main-sequence stars allowing for errors in the colors. Filled circles are Dwarf+Giant stars, open circles are PMS stars, and squares are Class I sources. See Tables 1 and 2 for details.

The analysis of results involved checking for correlations between the polarimetric and spectral data. The degree of polarization appears to be well-correlated with near-IR colors (Fig. 4). The near-IR polarization-to-extinction efficiency is consistent with that caused by aligned dust grains in the dense interstellar medium. The sources with $P/\delta P \geq 3$ in P vs. $(H - K_s)$ are mostly distributed below the empirical relation (Jones 1989) for the upper limit, $P_{\rm max}$, of interstellar polarization.

$$P_{\rm max}(\%) = 100 \tanh \left\{ 1.5\, E(H-K) \times \frac{1-\eta}{1+\eta} \right\} \tag{9}$$

where η = 0.875 (Jones 1989), and $E(H-K)$ is the reddening owing to extinction. $E(H-K)$ is calculated assuming that their polarizations are dominated by dichroic extinction without intrinsic polarization. Since extended and scattered light can enhance the polarization, we can detect candidate stars with intrinsic polarization (i.e., with circumstellar material) by selecting sources with larger polarizations than values, $P_{\rm max}$, estimated from the dichroic absorption due to foreground material.

We detected the HH 1-2 nebulosities as infrared reflection nebulae (IRNe) on our polarization images, but the polarimetric studies of the IRNe in the HH 1-2 region will be described elsewhere.

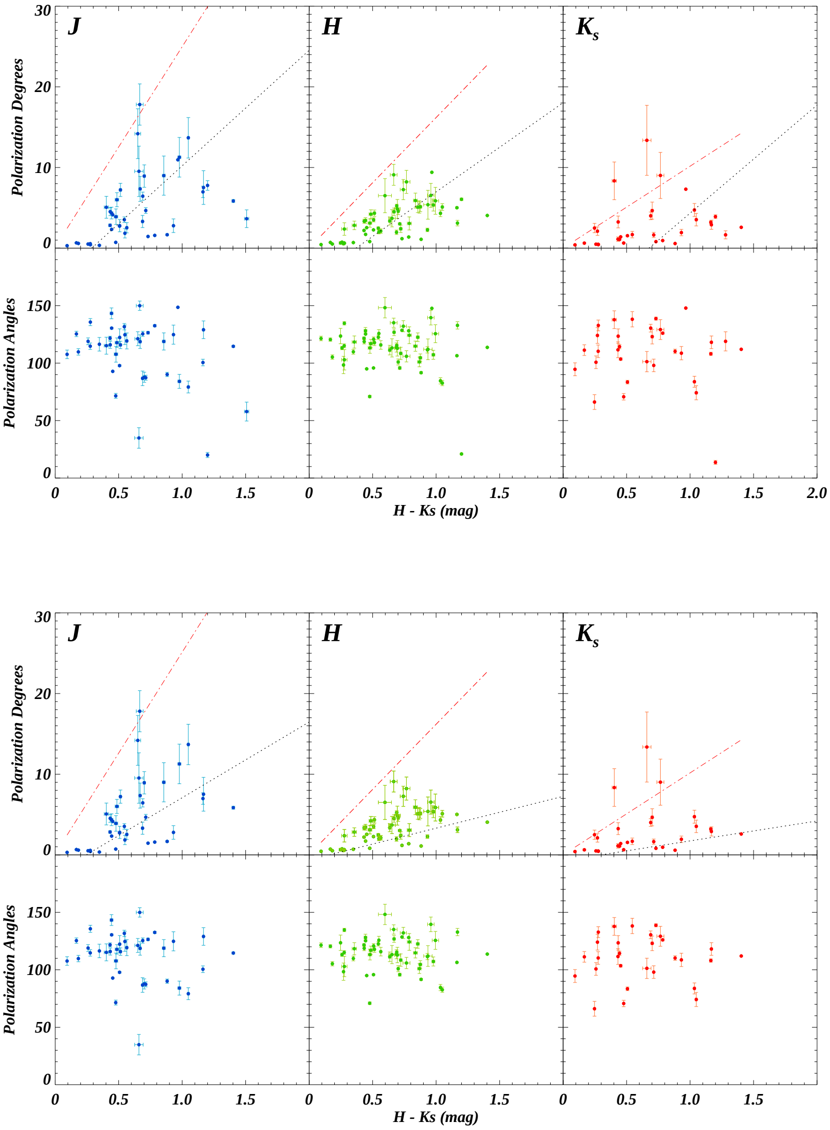

Fig. 4.— Observed J, H, and K_s polarization against H - K_s color for the HH 1-2 field sources. (Top panel) The results for the sources corresponds to $P/\delta P \geq 3$ for the 79 sources of Table 1. (Bottom panel) The results for the sources corresponds to $P/\delta P \geq 3$ for Dwarf+Giant stars of Table 1. The red dash-dotted line is observational upper limit ($P_{\max}$). and upper ones of the $P_{\max}$ may have intrinsic polarization. The black dotted line denotes the mean relationship between extinction and polarization for interstellar molecular clouds from Jones (1989). Note that linear fitting of the sources yields the slope of $\sim$4 for the H band, which is similar to the typical value for interstellar molecular clouds (Jones 1989). For the J and K_s bands, the slopes are $\sim$9 and $\sim$2, respectively.

4. DISCUSSION

4.1. The Direction of Magnetic Fields

The aperture polarimetry of stars provides important information on the direction of magnetic fields. If we assume the normal grain alignment, i.e., the spin axis of elongated dust grains aligned parallel to the magnetic fields (Davis & Greenstein 1951), the direction of magnetic fields projected onto the sky can be inferred from the direction of the polarization vectors of stars (Weintraub et al. 2000). Aperture polarization vector maps of point-like sources superposed on the I images of J, H, and K_s bands are shown in Figure 5. Figure 6 presents the histogram and gaussianfit for the polarization position angles of Dwarf+Giant stars in the HH 1-2 field. The peak angle of all histograms is $\sim 110°$. This direction of the aperture polarization is slightly inconsistant with that derived from the optical polarimetry (PA = 126°±6°, Warren-Smith & Scarrott 1999). Since PMS stars and Class I sources may be intrinsic polarization, we except for them.

Warren-Smith & Scarrott (1999) presented the no-filter linear polarization of eight stars in the HH 1-2 field, and suggested that non-spherical dust grains are strongly aligned in the magnetic field that permeates through the observed region ($10' \times 10'$), although the overall spread in orientations amounts to ~54°. So there are substantial local variations in the field direction, or the alignment achieved has not always been perfect. We note that star #2 and star #4 of Warren-Smith & Scarrott (1999) are saturated in our data, but we have more stars which they cannot detect because of the large amount of extinction. It means that our results is statistically more significant. We can compare star #5 of Warren-Smith & Scarrott (1999) with ours. They presented polarization degree of star #5 is 5.0±0.4 (%), and position angle is 153°±6°. In comparison, our results are 9.41±0.03 (%) and 147.66°±0.08°, respectively in the H band.

To see whether there is a systematic trend or not, we divided the HH 1-2 field by 16 (4 $\times 4$) subregions. The sample sources were selected by $P/\delta P \geq 3$ for each band among Dwarf+Giant stars to reduce uncertainty from the sources with intrinsic polarization or small signal-to-noise ratio. The average position angles of each subregion have no systematic trend (Fig. 7).

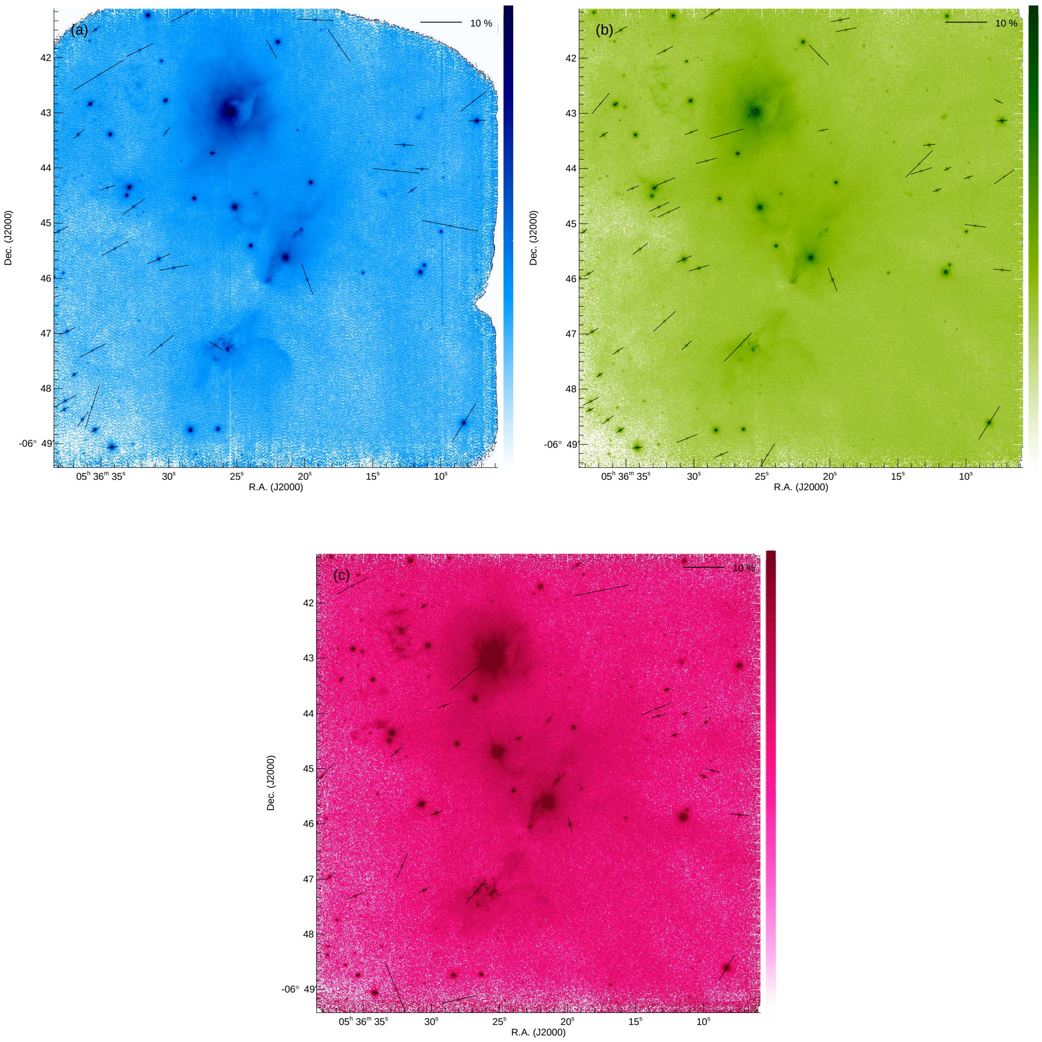

Fig. 5.— Stokes I images of J band (a), H band (b), and K_s band (c). The lines are polarization vectors, and the length of the plotted vectors is proportional to the polarization degrees (%).

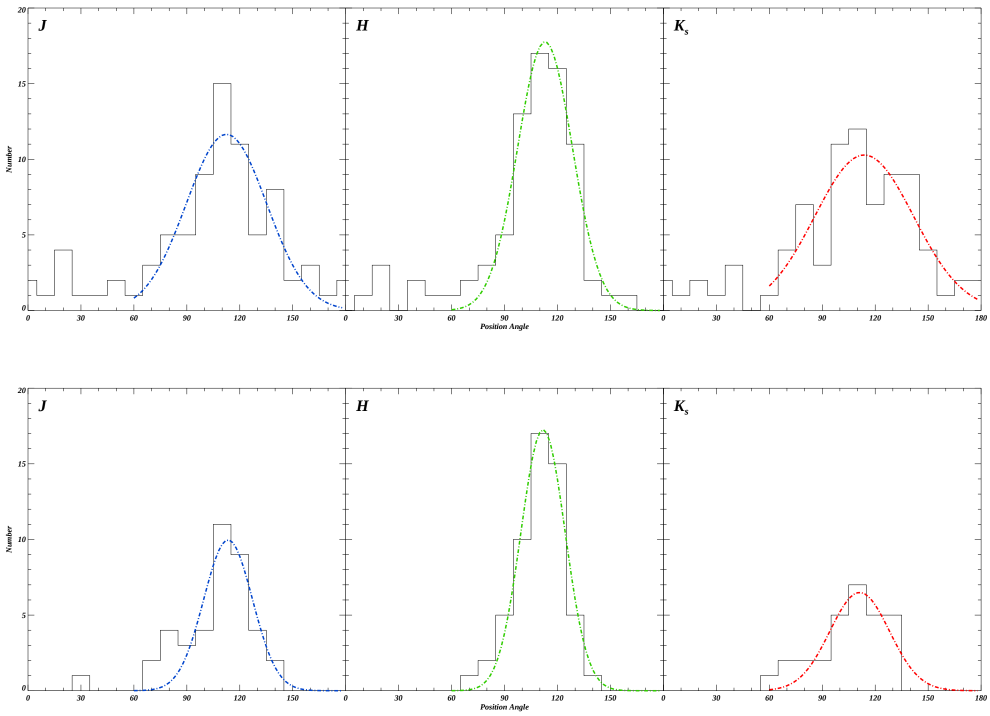

Fig. 6.— The histogram of position angles in the J, H, and K_s bands, respectively. The peak is $\sim 110°$. (Top panel) The histogram of 79 sources whose photometric uncertainties are less than 0.1 mag. The dispersions are $\sim 20°$, $\sim 15°$, and $\sim 30°$. (Bottom panel) The histogram of 40, 56, and 29 sources selected by $P/\delta P \geq 3$ among Dwarf+Giant stars. The dispersions are $\sim 13°$, $\sim 12°$, and $\sim 16°$.

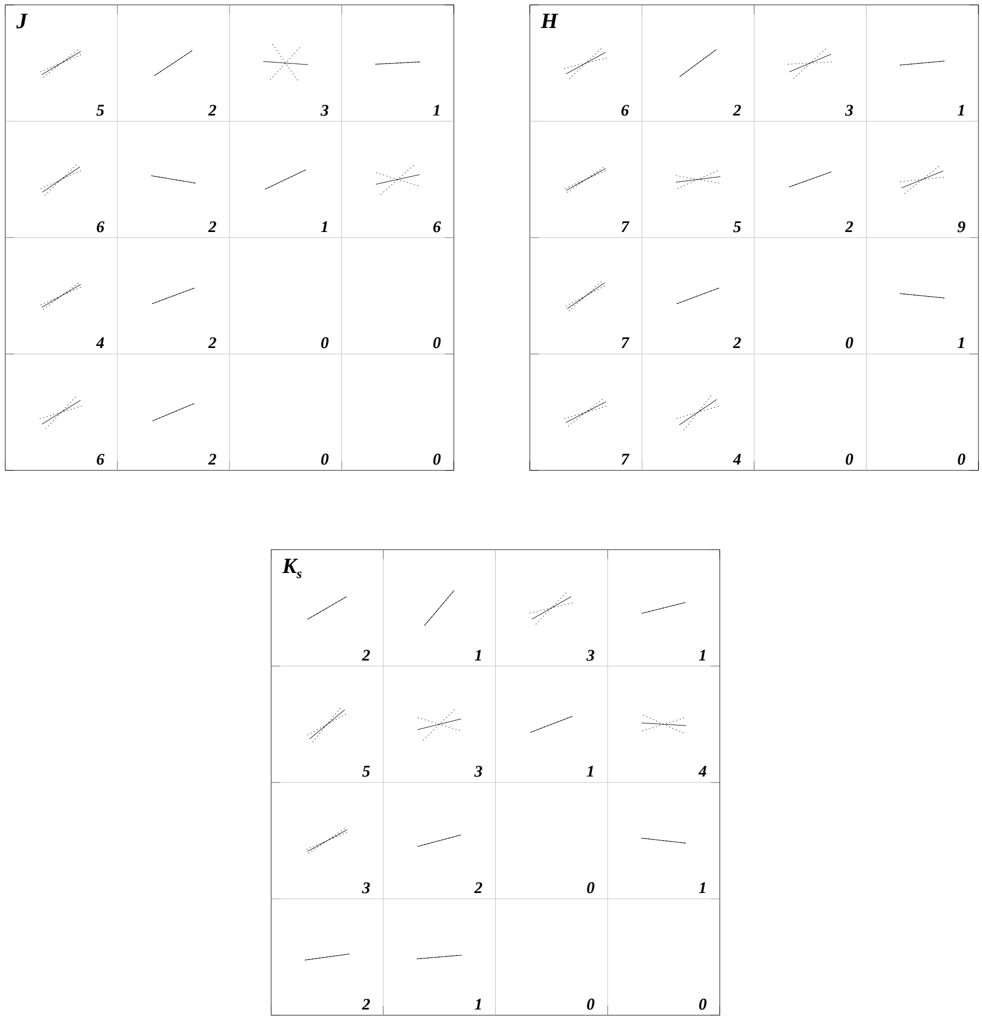

Fig. 7.— The distribution of polarization position angles for the HH 1-2 field sources in the J, H, and K_s bands, respectively. The number in each box means the number of sources selected by $P/\delta P \geq 3$ for each band among Dwarf+Giant stars in each subregion.

4.2. Estimation of the Magnetic Field Strength

Although the magnetic field strength cannot be directly inferred from the polarization of dust emission, the Chandrasekhar-Fermi (CF) formula modified with a factor of 0.5 can be used to estimate the magnetic field strength in the plane of the sky (Chandrasekhar & Fermi 1953; Ostriker et al. 2001). A simple estimate of the field strength is obtained by assuming that the field is in equipartition with the turbulent pressure of the gas. The projected field strength, B_p, can be expressed as

$$B_p = 0.5\sqrt{4\pi\overline{\rho}}\ \frac{\delta v_{los}}{\delta\theta}, \tag{10}$$

where $\overline{\rho}$ is the mean density, δv_{los} is the rms line-of-sight velocity, and $\delta\theta$ is the dispersion of polarization angles. The linewidth (FWHM), $\delta v = \sqrt{8ln2}\ \delta v_{los}$, of 2.7 km s^{-1} was from on the observations of $C^{18}O$ $J = 1 \rightarrow 0$ (Takaba et al. 1986). The column density assumed to estimate B_p in HH 1-2 field, N_{H_2} is 2.5×10^{22} cm^{-2}, is from the detection of the $J = 1 \rightarrow 0$ transitions in CO and ^{13}CO with the size 2 pc (Takaba et al. 1986). Thus the number density n_{H_2} is 4×10^3 cm^{-3}. The $\delta\theta$, 12°, is from the gaussian fit of bottom panel of Figure 6. We derive that the magnetic field strength in the HH 1-2 field in the plane of the sky is about 100 μG.

Many previous studies estimated the magnetic field strength using the dispersion in polarization angles (Garay et al. 1989; Gonatas et al. 1990; Lai et al. 2008; Alves et al. 2008; Andersson & Potter 2005). Gonatas et al. (1990) estimated the magnetic field strength to be between 0.7 and 4 mG in the far-infrared polarization of the Orion nebula. Lai et al. (2008) suggested that the magnetic field is strong ($\gtrsim$ 2 mG) in the NGC 2024 FIR 5 molecular core. Alves et al. (2008) represented that the plane of the sky magnetic field strength was estimated to vary from about 17 μG in the B59 region to about 65 μG in the bowl. Andersson & Potter (2005) found a plane-of-the-sky magnetic field for the Coalsack cloud of 93 μG. The derived magnetic field strength in the HH 1-2 field is larger than those measured for most diffuse clouds (Myers et al. 1995), but fall within those measured for molecular clouds (Crutcher 1999).

Goodman et al. (1995) on the other hand suggest that the polarization map of background starlight cannot reliably trace the magnetic field associated with the dense interior of the dark cloud, since much of the dust in the dark cloud is extinguishing background starlight significantly, but not polarizing it efficiently. The CF relation between the dispersion in the direction of polarization angles and magnetic field strength is modified in realistic simulations by line-of-sight and beam size averaging (Zweibel 1990; Myers & Goodman 1991; Heitsch et al. 2001; Ostriker et al. 2001). Therefore, using the CF relation allows us to derive estimates of the strength of the plane-of-the-sky magnetic field strength in the gas (Andersson & Potter 2005), the reliability depends on the relative kinetic and magnetic energy densities of the medium, the covering factor of the clumps, and the degree of ionization (Zweibel 1990).

4.3. Polarization of PMS Stars and Class I Sources

In section 4.1, we measured the direction of magnetic field except for PMS stars and Class I sources, because they may have circumstellar disks that cause intrinsic polarization. Figure 8 shows the histogram of the position angles for PMS stars and Class I sources. We can check there is intrinsic polarization.

4.4. Magnetic Field Direction and Outflow Axis

The direction of magnetic field is significantly inclined ($\sim$40°) to the HH 1-2 outflow axis (PA=149°). For the difference between the direction of magnetic field and outflow/jet axis, we suggest the following explanations. First, the axes of accretion disks are unequal for each star associated with binary systems (Reipurth 2000). For example, VLA1 and VLA2 are driving sources of HH 1-2 and HH 144-145, respectively. Although VLA2 is also very young and only a few arcseconds from VLA1, the outflow axis of HH 1-2 is inclined 50° to that of HH 144-145. Second, the turbulence nothing more than the gas flow resulting from random motions at many scales exists in molecular cloud (Elmegreen 2000; MacLow & Klessen 2004). In the neighborhood of HH 1-2, there are at least four other outflows with known driving sources: HH

35, HH 144, HH 146, and HH 147 (Table 3), but these outflows in this small region seem not to follow the local cloud magnetic field (Fig. 8).

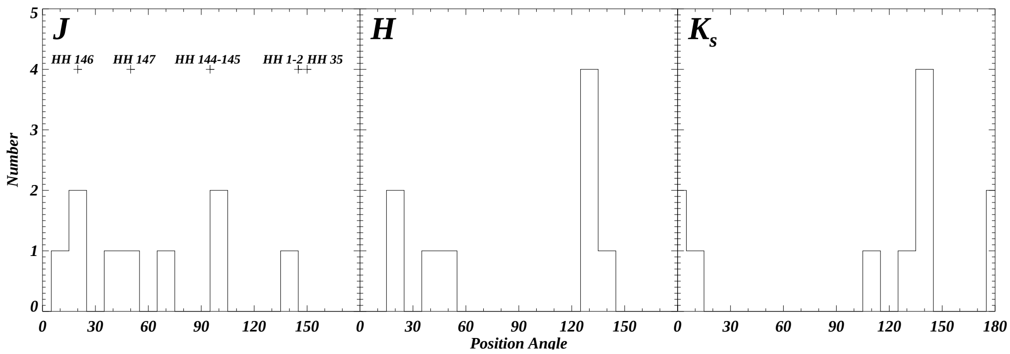

Fig. 8.— The histogram of polarization position angles for PMS stars and Class I sources in the J, H, and K_s bands, respectively. There is no a peak toward a particular angle. The five HH objects shown in the J band are from Table 3.

Table 3. The outflow axis of HH objects in the HH 1-2 field

Object	P.A.[a]	Driving Source	References
HH 1-2	325°	VLA1	Bally et al. 2002
HH 3	...	unknown	Dopita et al. 1982
HH 35	330°	V380 Ori	Eislöffel et al. 1994
HH 144-145...	275°	VLA2	Eislöffel et al. 1994, Reipurth et al. 1993
HH 146	200°	VLA4 (star No. 3 of Reipurth et al. 1993)	Reipurth et al. 1993
HH 147	230°	star No. 3 of Strom et al. 1985	Eislöffel et al. 1994
HH 148	...	unknown	Reipurth et al. 1999

[a] Position angle of the outflow axis

5. SUMMARY

We conducted deep and wide-field JHK_s imaging polarimetry toward the $\sim$8′ × $\sim$8′ region around HH 1-2 in the star-forming cloud L1641. The main conclusions in this study are summarized as follows:

1. Aperture polarimetry of the point-like sources in the HH 1-2 field in the JHK_s bands is made for the first time. The number of detected point-like sources in all three bands is 79. The degree of polarization of the point-like sources is as high as $\sim$9% in the H band.

2. Most of the near-IR polarizations of point-like sources can be explained by dichroic polarization. We found that several stars show stronger degree of polarization than expected from extinction.

3. The average position angle of the projected magnetic fields is about 110° with a dispersion of 12° in the H band.

4. The magnetic field strength estimated with the modified Chandrasekhar-Fermi formula is about 100 μG.

REFERENCES

Aitken, D. K., Smith, C. H., Moore, T. J. T., & Roche, P. F. 1995, MNRAS, 273, 359

Alves, F. O., Franco, G. A. P., & Girart, J. M. 2008, A&A, 486, 13

Andersson, B.-G., & Potter, S. B. 2005, MNRAS, 356, 1088

Bally, J., Stark, A. A., Wilson, R. W., & Langer, W. D. 1987, ApJ, 312, 45

Bessell, M. S., & Brett, J. M. 1988, PASP, 100, 1134

Casali, M. M. 1995, MNRAS, 277, 1385

Castets, A., Duvert, G., Dutrey, A., Bally, J., Langer, W. D., & Wilson, R. W. 1990, A&A, 234, 469

Cernicharo, J., Bujarrabal, V., & Lucas, R. 1991, A&A, 249, 27

Chandrasekhar, S., & Fermi, E. 1953, ApJ, 118, 116

Choi, M., & Zhou S. 1997, ApJ, 477, 754

Correia, J. C., Griffin, M., & Saraceno, P. 1997, A&A, 322, 25

Crutcher, R. M. 1999, ApJ, 520, 706

Davis, L. J., & Greenstein, J. L. 1951, ApJ, 114, 206

Dopita, M. A., Binette, L., & Schwartz, R. D. 1982, ApJ, 261, 183

Eislöffel, J., Mundt, R., & Bohm, K. H. 1994, AJ, 108, 1042

Elmegreen, B. G., 2000a, ApJ, 530, 277

Elmegreen, B. G., 2000b, ApJ, 539, 342

Elmegreen, B. G., 2000c, MNRAS, 311, L5

Fukui, Y., & Mizuno, A. 1991, in Fragmentation of Molecular Clouds and Star Formation, ed. E. Falgarone, F. Boulanger, & G. Duvert (Dordrecht: Kluwer), 275

Garay, G., Moran, J. M., & Haschick, A. D. 1989, ApJ, 338, 244

Gonatas, D. P. et al. 1990, ApJ, 357, 132

Goodman, A. A., Jones, T. J., Lada, E. A., & Myers, P. C. 1995, ApJ, 448, 748

Haro, G. 1952, ApJ, 115, 572

Heitsch, F., Zweibel, E. G., Mac Low, M.-M., Li, P., & Norman, M. L. 2001, ApJ, 561, 800

Herbig, G. H. 1951, ApJ, 113, 697

Herbig, G. H., & Jones, B. F. 1981, AJ, 86, 1232

Heyer, M. H., Morgan, J., Schloerb, F. P., Snell, R. L., & Goldsmith, P. F. 1992, ApJ, 395, 99

Hirota, T. et al. 2007, PASJ, 59, 897

Jones, T. J. 1989, ApJ, 346, 728

Kandori, R. et al. 2006, Proc. SPIE, 6269, 159

Kandori, R. et al. 2007, PASJ, 59, 487

Kutner, M. L., Tucker, K. D., Chin, G., & Thaddeus, P. 1977, ApJ, 215, 521

Lai, S. P. et al. 2008, AJ, 566, 925

Lazarian, A. 2007, J. Quant. Spectrosc. Radiat. Transfer, 106, 225

Mac Low, M.-M. & Klessen, R. S. 2004, Rev. Mod. Phys., 76, 125

Maddalena, R. J., Morris, M., Moscowitz, J., & Thaddeus, P. 1986, ApJ, 303, 375

McGregor, P. J., Harrison, T. E., Hough, J. H., & Bailey, J. A. 1994, MNRAS, 267, 755

Menten, K. M., Reid, M. J., Forbrich, J., & Brunthaler, A. 2007, A&A, 474, 515

Meyer, M. R., Calvet, N., & Hillenbrand, L. A. 1997, AJ, 114, 288

Mouschovias, T., & Ciolek, G. 1999, in The Origins of Stars and Planetary Systems, ed. C. Lada & N. Kylafis (Dordrecht: Kluwer), 305

Myers, P. C., & Goodman, A. A. 1991, ApJ, 373, 509

Myers, P. C., Goodman, A. A., Gusten, R., & Heiles, C. 1995, ApJ, 442, 177

Nagayama, T. et al. 2003, Proc. SPIE, 4841, 459

Nakano, M., Wiramihardja, S. D., & Kogure, T. 1995, PASJ, 47, 889

Ostriker, E. C., Stone, J. M., & Gammie, C. F. 2001, AJ, 546, 980

Pravdo, S. H., Rodriguez, L. F., Curiel, S., Canto, J., Torrelles, J. M., Becker, R. H., & Sellgren, K. 1985, ApJ, 293, 35

Reipurth, B. 2000, AJ, 120, 3177

Reipurth, B., Heathcote, S., Roth, M., Noriega-Crespo, A., & Raga, A. C. 1993, ApJ, 408, L49

Rodríuez, L. F., Ho, P. T. P., Torrelles, J. M., Curiel, S., & Cantó, J. 1990, ApJ, 352, 645

Sakamoto, S., Hasegawa, T., Hayashi, M., Morino, J.-I., & Sato, K. 1997, AJ, 481, 302

Sakamoto, S., Hayashi, M., Hasegawa, T., Handa, T., & Oka, T. 1994, ApJ, 425, 641

Sandstrom, K. M., Peek, J. E. G., Bower, G. C., Bolatto, A. D., & Plambeck, R. L. 2007, ApJ, 667, 1161

Sato, S., Tamura, M., Nagata, T., Kaifu, N., Hough, J., McLean, I. S., Garden, R. P., & Gatley, I. 1988, MNRAS, 230, 321

Shu, F. H. 1999, ApJ, 525, 347

Stetson, P. B. 1987, PASP, 99, 191

Strom, S. E., Strom, K. M., Grasdalen, G. L., Sellgren, K., Wolff, S., Morgan, J., Stocke, J., & Mundt, R. 1985, AJ, 90, 2281

Strom, K. M., Strom, S. E., Wolff, S. C., Morgan, J., & Wenz, M. 1986, ApJS, 62, 39

Takaba, H., Fukui, Y., Fujimoto, Y., Sugitani, K., Ogawa, H., & Kawabata, K. 1986, A&A, 166, 276

Tatematsu, K. et al. 1993, ApJ, 404, 643

Torrelles, J. M., Gomez, J. F., Ho, P. T. P., Rodriguez, L. F., Anglada, G., & Canto, J. 1994, ApJ, 435, 290

Vrba, F. J., Strom, S. E., & Strom, K. M. 1988, AJ, 96, 680

Wardle, J. F. C., & Kronberg, P. P. 1974, ApJ, 194, 249

Warren-Smith, R. F., & Scarrott, S. M. 1999, MNRAS, 305, 875

Weintraub, D. A., Goodman, A. A., & Akeson, R. L. 2000, in Protostars and Planets IV, ed. V. Mannings, A. P. Boss, & S. S. Russell (Tucson: Univ. Arizona Press), 247

Whittet, D. C. B. 1992, Dust in the Galactic Environment (Bristol: IOP), 67

Whittet, D. C. B., Gerakines, P. A., Hough, J. H., & Shenoy, S. S. 2001, ApJ, 547, 872

Zweibel, E. G. 1990, ApJ, 348, 186

This preprint was prepared with the AAS LaTeX macros v5.2.